



Enhanced multiscale modeling of macroscopic and microscopic residual stresses evolution during multi-thermo-mechanical processes



X.X. Zhang^a, D. Wang^a, B.L. Xiao^a, H. Andrä^b, W.M. Gan^c, M. Hofmann^d, Z.Y. Ma^{a,*}

^a Shenyang National Laboratory for Materials Science, Institute of Metal Research, Chinese Academy of Sciences, 72 Wenhua Road, Shenyang 110016, China

^b Fraunhofer Institute for Industrial Mathematics, Fraunhofer-Platz 1, Kaiserslautern 67663, Germany

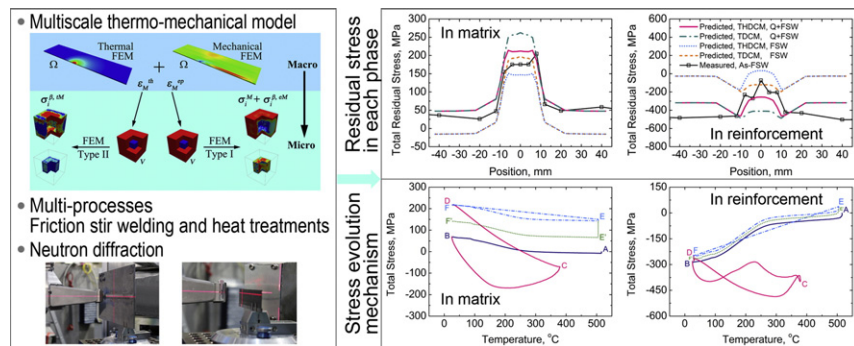
^c German Engineering Materials Science Centre, Helmholtz-Zentrum Geesthacht, D-21502 Geesthacht, Germany

^d Technische Universität München, Forschungsneutronenquelle Heinz Maier-Leibnitz (FRM II), D-85747 Garching, Germany

HIGHLIGHTS

- A multiscale model is developed for predicting residual stresses in MMCs during multi-thermo-mechanical processes.
- The multiscale model is capable of handling initial stresses and integrates temperature history dependent constitutive model.
- Integrating both multiscale modeling and neutron diffraction, the stress evolution mechanism in MMCs is captured.
- The multiscale model provides promising predictions of residual stresses in MMCs during complex processes.

GRAPHICAL ABSTRACT



ARTICLE INFO

Article history:

Received 13 October 2016

Received in revised form 7 November 2016

Accepted 16 November 2016

Available online 22 November 2016

Keywords:

Residual stress
Metal matrix composites
Neutron diffraction
Friction stir welding
Multiscale model

ABSTRACT

After several decades, it is still difficult to predict “macroscopic and microscopic (M-m)” residual stresses (RSEs) in metal matrix composites (MMCs) after welding. In this work, an enhanced multiscale model is developed to predict the evolution of M-m RSEs in MMCs during several thermo-mechanical processes including welding. This multiscale model is capable of handling non-zero initial M-m RSEs and integrates the temperature history dependent constitutive model (THDCM) at both macroscale and microscale. Meanwhile, thermal source model of friction stir welding (FSW) is integrated. The extension to other welding thermal source is straightforward. This multiscale model is used to study the generation, inheritance, and evolution of M-m RSEs in a SiC/Al composite during quenching, FSW and post-welding heat treatment (PWHT). The effects of initial M-m RSEs and material constitutive models on the prediction of M-m RSEs are systematically assessed. It is found that using the THDCM and taking into account the initial RSEs, this multiscale model shows the best predictions of RSEs in the FSW joint of MMCs. The predictions agree with the neutron diffraction measurements reasonably well. It is found that the reduction of RSEs during PWHT is mainly caused by the stress relaxation during the solution treatment stage.

© 2016 Elsevier Ltd. All rights reserved.

1. Introduction

Generally, residual stresses (RSEs) are introduced by an inhomogeneous deformation in thermal, mechanical or thermo-mechanical

* Corresponding author.

E-mail address: zyyma@imr.ac.cn (Z.Y. Ma).

processes, e.g. heat treatments, material forming processes and welding [1–5]. The existence of residual stress may lead to an unexpected stress field across a structure when an external load is applied [6]. Such unexpectedness raises risks to structural performances [7], such as causing geometrical distortions [8], triggering microscale cracking [9] and exacerbating stress corrosion cracking [7]. In metal matrix composites (MMCs) RSEs include both macroscopic and considerable microscopic (originating from elastic mismatch, thermal and plastic misfit between matrix and reinforcement) stresses [7,10,11]. Therefore, quantitative characterization of “macroscopic and microscopic (M-m)” RSEs in MMCs is critical.

The generation and evolution of RSEs in MMCs has been investigated in some ideal cases over the last couple of years [9,12–16]. Most of these investigations utilize modern techniques such as neutron diffraction or synchrotron X-ray diffraction. For instance, we developed a new method for determining M-m RSEs in MMC welds via neutron diffraction [11]. However, for many engineering cases, e.g. large-sized MMC structures, accurate determination of RSEs based on these methods still may be impossible. Therefore, developing a reliable model to predict M-m RSEs in MMCs is crucial for assessing the structural integrity.

Many models have been developed to predict RSEs in MMCs, such as the Eshelby type models [10,17,18], unit cell based microscale finite element (FE) models [19] and macroscale FE models that simply treat MMCs as homogeneous effective mediums ignoring the multiphase feature [20]. These models deal with either the microscopic RS or the macroscopic RS individually, but do not consider them together.

Multiscale methods combine macroscale models, which are capable of handling initial and boundary conditions of real-life engineering problems, with microscale models, which take into account the microstructure and microscale constitutive models [21–26]. According to the scale coupling methods, multiscale models can be classified into two basic categories: concurrent and hierarchical. Besides, several mixed multiscale models are also established, such as the semiconcurrent and the hybrid-semiconcurrent multiscale models [24,27–29]. So far, developing any kind of these advanced multiscale models to predict the M-m RSEs in MMCs after complex thermo-mechanical processes is still challenging.

This work presents a possible solution to predict M-m RSEs in MMCs after complex thermo-mechanical processes. For this purpose, a new enhanced hierarchical multiscale model is established based on the models proposed in our previous works [29,30]. New developments include:

- 1) The temperature dependent friction coefficient based thermal source model developed in our previous works is integrated [31, 32]. This offers the present multiscale model a new ability to handle friction stir welding (FSW) process. Extension of this ability to other welding processes is straightforward.
- 2) Temperature history dependent constitutive models (THDCMs) at both the macroscale and the microscale are implemented. This significantly improves the accuracy when considering age-hardened alloys and MMCs. Our original models [29,30] are based on temperature dependent constitutive models (TDCMs), which usually overestimate the RSEs for age-hardened materials [33].
- 3) Non-zero initial RSEs are taken into account. This grants the computation ability of the multiscale model from a single thermo-mechanical process to multi-thermo-mechanical processes for MMCs.

The generation, inheritance, and evolution of M-m RSEs in a 17 vol.% SiCp/2009Al-T4 composite during quenching, FSW and post-welding heat treatment (PWHT) are investigated using this new enhanced hierarchical multiscale model. The effects of initial RSEs and material constitutive models on the prediction of M-m RSEs are systematically assessed. Neutron diffraction is conducted to examine the accuracy of the model predictions by following the procedure proposed in our previous work [11].

2. Theoretical and modeling approach

The basic 3D multiscale thermo-mechanical framework for multiphase materials has been reported in our previous publications [29,30, 34,35] and is further developed in this work. The first development of the multiscale model is taking into account the heat generation model for FSW modeling. The heat generation rate s is computed by

$$s = \mu(T)p \left(\frac{2\pi\omega}{60}r + \frac{v}{60} \sin\theta \right) \tag{1}$$

where $\mu(T)$ is a temperature dependent friction coefficient based on our previous works for FSW [31,32], p pressure, ω rotation rate of FSW, r radius, v advancing speed of FSW, θ angle. For other welding processes, e.g. fusion welding, the heat generation rate s can be replaced by corresponding formulations.

At the microscale, the matrix is elastoplastic and the reinforcement is linear elastic. In complex thermo-mechanical processes, like welding, high temperature exposure causes phase transformation in age-hardened material, thereby changing the mechanical properties. To model this behavior, the temperature rate \dot{T} has to be considered. Then, the second development of the multiscale model, the general yield condition of the THDCM reads

$$f_m(\boldsymbol{\sigma}_m, p_m, T, \dot{T}) = \sqrt{3/2} \|\text{dev}[\boldsymbol{\sigma}_m(p_m, T, \dot{T})]\| - \sigma_m(p_m, T, \dot{T}) \tag{2}$$

where script m denotes microscale, $\boldsymbol{\sigma}$ is the stress tensor, p indicates the accumulated plastic strain, $\|\bullet\|$ denotes the norm of the indicated tensor, $\text{dev}(\bullet)$ the deviator of the indicated tensor, $\sigma(\bullet)$ the yield stress. The Voce type isotropic hardening rule reads [36]

$$\sigma_m(p_m, T, \dot{T}) = \sigma_m^\infty(T, \dot{T}) + h_m p_m + [\sigma_m^0(T, \dot{T}) - \sigma_m^\infty(T, \dot{T})] \exp(-l_m p_m) \tag{3}$$

where σ^0 is the initial yield strength, σ^∞ the ultimate strength, both h and l are the material constants.

At the macroscale, MMC is modeled as a homogeneous effective medium and described by a von-Mises type elastoplastic constitutive law based on the pre-computed effective properties via computational homogenizations [35]. The macroscopic yield function is

$$f_M(\boldsymbol{\sigma}_M, p_M, T, \dot{T}) = \sqrt{3/2} \|\text{dev}[\boldsymbol{\sigma}_M(p_M, T, \dot{T})]\| - \sigma_M(p_M, T, \dot{T}) \tag{4}$$

where script M denotes macroscale, the isotropic hardening function $\sigma_M(p_M, T, \dot{T})$ is fitted utilizing spline interpolation function of $\langle \sigma_{Mises} \rangle$ with respect to $\langle p \rangle$, T and \dot{T} [35].

For multi-thermo-mechanical processes, the microscopic RSEs induced during one previous process act as initial stresses $\boldsymbol{\sigma}_m^{initial}$ for the structures at the outset of following process. These initial stresses can simply be added on to the definition of Hooke's law to compute the microscale stress tensor

$$\boldsymbol{\sigma}_m = \mathbf{E}_m \boldsymbol{\epsilon}_m^e + \boldsymbol{\sigma}_m^{initial} \tag{5}$$

where \mathbf{E} is the elastic stiffness tensor, $\boldsymbol{\epsilon}^e$ the elastic strain tensor. This is the third development of the multiscale model. Similarly, the computation of stress tensor at the macroscale follows

$$\boldsymbol{\sigma}_M = \mathbf{E}_{eff} \boldsymbol{\epsilon}_M^e + \boldsymbol{\sigma}_M^{initial} \tag{6}$$

where \mathbf{E}_{eff} is the effective elastic stiffness tensor.

Table 1
Coordinates of ten macro-micro points.

Macro-micro point	Coordinates (mm)		
	X	Y	Z
P0	0	150	1.55
P1	2	150	1.55
P2	4	150	1.55
P3	6	150	1.55
P4	8	150	1.55
P5	10	150	1.55
P6	12	150	1.55
P7	22	150	1.55
P8	32	150	1.55
P9	42	150	1.55

3. Computational aspect

3.1. Numerical solution method

The multiscale model is composed of one macroscale boundary value problem (BVP) and several microscale BVPs at macro-micro points. In this work, ten macro-micro points are investigated by type I and II microscale BVPs. The coordinates of the macro-micro points are listed in Table 1 and illustrated in Fig. 1(a). The basic numerical solution method of a hierarchical multiscale model is described in our previous work [30]. In this work, the multiscale model and its solution procedure are summarized as:

- 1) The residual vector and the stiffness matrix for all macroscale integration points are computed via homogenized constitutive model based on unit cell (UC) and constitutive models of the metal matrix and the reinforcement. The detailed method for homogenizing the constitutive model was reported in [35].
- 2) The macroscale BVP is constructed based on the homogenized constitutive model and macroscale boundary conditions (BCs) according to the detailed physical problem.
- 3) Two types of microscale BVPs are constructed for separating the different microscopic RSes based on the kinematic uniform boundary conditions (KUBC). In type I microscale BVP, the macroscale elastoplastic strain tensor is used to construct the KUBC for separating the elastic mismatch RS from the macroscopic RS. In type II microscale

BVP, the macroscale thermal strain tensor is used to construct the KUBC for computing the thermal misfit RS.

For more details, one can refer to our previous work [30].

3.2. Numerical experiments

The computational domains at the macroscale and the microscale used in this work are shown in Fig. 1. At the microscale a UC is used in this work. A 17 vol.% SiCp/2009Al composite is studied. Three classes of multi-thermo-mechanical process chains are modeled, which are briefly summarized as:

- 1) FSW: The initial stresses at the macroscale and microscale are set to zero.
- 2) Previous quenching + FSW (Q + FSW): M-m RSes from the previous quenching process (from 516 °C to 25 °C) are modeled firstly and then set as the initial stresses for modeling the FSW process.
- 3) Previous quenching + FSW + post quenching (Q + FSW + PQ): M-m RSes from the previous quenching process are modeled firstly and then set as the initial stresses for modeling the FSW process. The predicted M-m RSes from the FSW process are set as the initial stresses for modeling the post quenching process (from 505 °C to 25 °C).

The multiscale modeling is carried out with software MSFESL developed at our laboratory [29,30,34,35].

4. Experiments

4.1. Material and FSW

17 vol.% SiCp/2009Al-T4 composite plates 3.1 mm in thickness were used. The 2009Al matrix has a nominal composition of Al-4.0Cu-1.4 Mg (wt.%) and SiC particles have an average size of 7 μm. The composite was fabricated via powder metallurgy (PM) and hot rolled into plates at 480 °C. The composite plates were subjected to T4 treatment (solution treatment of 1 h at 516 °C, water quenching and natural aging of 7 days).

300 × 75 × 3.1 mm³ sized plates were welded parallel to the rolling direction using FSW, with a welding speed of 150 mm/min and a rotational rate of 1000 rpm. A cermet tool with a shoulder 14 mm in diameter and a cylindrical pin 5 mm in diameter and 2.7 mm in length was used. Two same welded samples were made. One is an as-FSW sample and another was subsequently subjected to PWHT (solution treatment

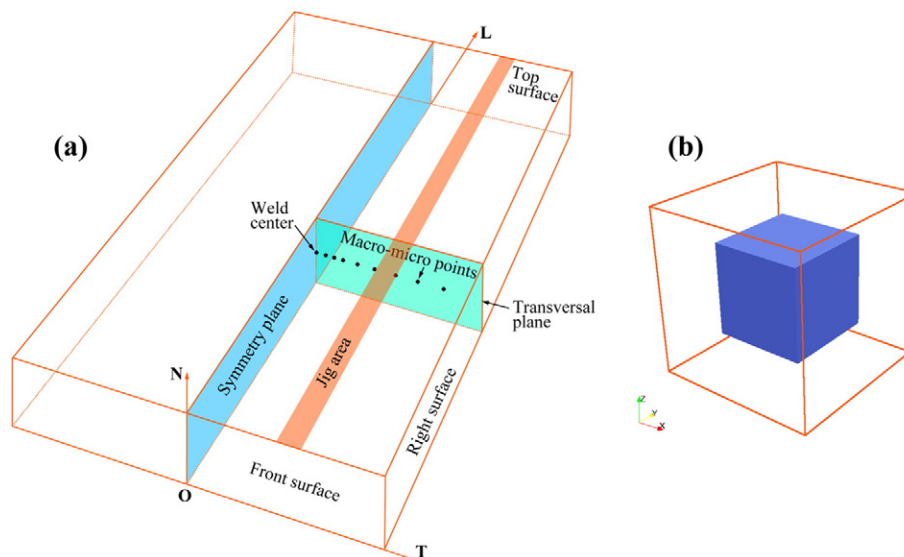


Fig. 1. Geometry models used in the multiscale simulation: (a) MMC plate, only the right half is modeled. Symmetry boundary conditions are imposed on the symmetry plane. (b) Unit cell (UC) model. The mean diameter of particles is 7 μm.

of 2 h at 505 °C, water quenching and natural aging of 7 days). Optical microscopic examination was carried out on the transverse section of the welds, where the specimens were mechanically polished and etched by Keller's reagent. The temperature history was recorded by embedding the thermocouple at the location of macro-micro point P2.

4.2. Neutron diffraction measurements

A new method of determining M-m RSEs in MMC welds via neutron diffraction has been developed recently in our previous work and more experimental details can be found therein [11]. To measure the phase specific residual strains, a weld sample, together with a comb sample of the weld and the reinforcement (SiC) powder sample are tested. The residual strains are then mapped to multiscale RSEs based on the Bragg equation and the equilibrium condition of microscopic stresses.

5. Results and discussion

The notation used for M-m RSEs here is consistent with reference [30]. The superscripts *ep*, *th*, *eM*, and *tM* denote elasto-plastic, thermal, elastic mismatch, and thermal misfit, respectively. The superscript β denotes *ma* or *pa*. Superscripts *ma* and *pa* denote matrix and particle, respectively. Letters *L*, *T*, and *N* denote longitudinal, transversal and normal, respectively. Hence, for instance, σ_L^M denotes longitudinal component of macroscopic RS, and $\sigma_L^{ma.eM}$ denotes longitudinal component of elastic mismatch RS in the matrix.

5.1. Microstructures

Fig. 2(a) shows that no macroscopic defects like voids, volumetric flaws or tunnels were observed in the FSW joint of the 17 vol.% SiCp/2009Al-T4 composite. The FSW joint can be typically divided into the nugget zone (NZ), the thermo-mechanically affected zone (TMAZ) and the heat-affected zone (HAZ). A typical onion structure was observed in the NZ. Fig. 2(b)–(e) show that the particle distribution in the NZ was more homogeneous than that in the base material (BM). It results from the severe plastic deformation during FSW and agrees with previous results [37–40]. Fig. 2(d) shows that in the center of the NZ more SiC particles tended to align along the *N* direction, also in agreement with previous references [11,39,40].

5.2. Temperature

Accurate thermal modeling is crucial for predicting welding RSEs. Fig. 3 shows that the predicted temperature history for the macro-

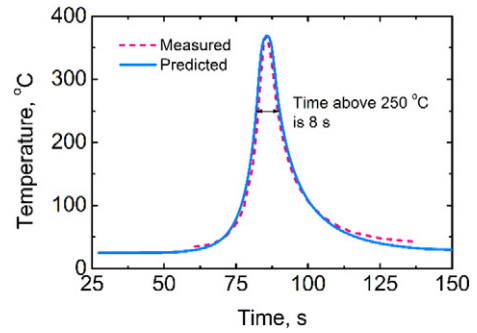


Fig. 3. Predicted and measured temperature history for macro-micro point P2.

micro point P2 agrees quite well with the experimentally measured one. Such a good agreement indicates that the FSW thermal model based on the temperature dependent friction coefficient is not only applicable to aluminum alloys [31,32], but also to other material classes such as MMCs. Fig. 4 shows the complete temperature histories at the weld center P0 defined in Table 1 from the previous quenching to the FSW and finally to the post quenching process. Temperature points A, B, C, D, E and F are defined in Fig. 4. M-m stress evolutions at these points will be discussed in Section 5.7.

5.3. Effects of material constitutive models

If one takes into account the real physical foundations for the evolution of temperature-microstructure-mechanical properties (T-M-MP) during welding, e.g. FSW, integrated modeling technique will be required [41]. It demands a model chain including (1) a thermal model, (2) a microstructure evolution model, which is extended for heterogeneous precipitation, and (3) a microstructure based strength and strain hardening model [42]. Such a complex technique is computationally costly. Furthermore, the precipitation state in 2xxx series Al alloys is more complex than that in 6xxx series Al alloys. Meanwhile, the addition of reinforcing particles like SiC in MMCs changes the precipitation behavior, which is not completely clear from the experimental observations compared to unreinforced Al alloys. Therefore, it is impossible to apply such an integrated model to compute the T-M-MP during welding. The practical way is to run an empirical THDCM, which reflects the physical foundations of T-M-MP and is more efficient.

Fig. 5 shows that using the THDCM improves the prediction of the tensile *L* macroscopic RS σ_L^M within the shoulder edge, while the TDCM overestimates the tensile RS σ_L^M , which agrees with previous

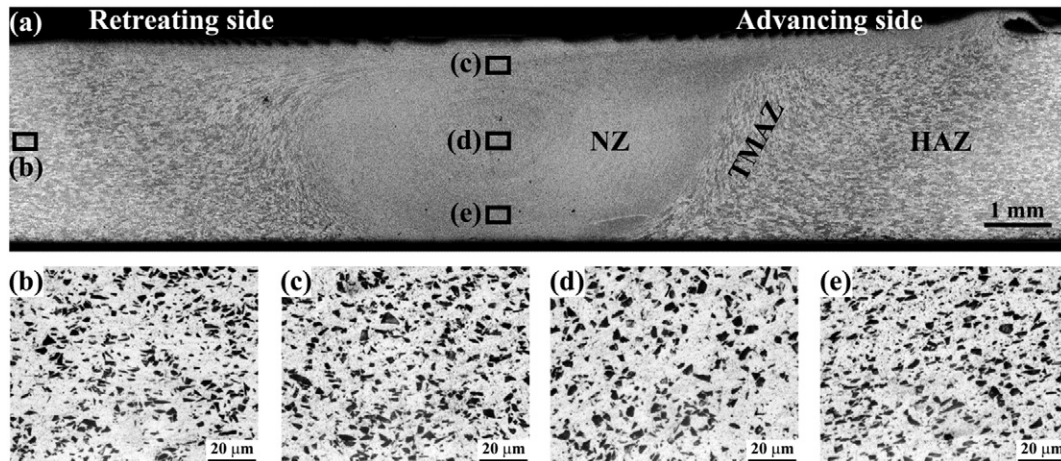


Fig. 2. Optical images of as-FSW sample: (a) overview of microstructure at the weld, (b) base material, (c) top of nugget zone, (d) center of nugget zone, (e) bottom of nugget zone. The locations of (b)–(e) are shown in (a). AS: advancing side, RS: retreating side.

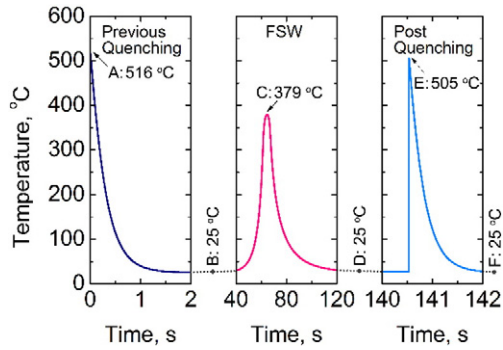


Fig. 4. The complete simulation of the thermal cycle for weld center P0 including three thermo-mechanical processes ((1) previous quenching, (2) FSW and (3) post quenching).

results [33]. In this area, plastic yield appears due to large heterogeneous thermal expansion and contraction during heating and cooling stage, respectively. The yield strength in the TDCM is higher than that in the THDCM during the cooling stage. Therefore, the possible plastic deformation occurring due to thermal contraction could not be well captured by the TDCM. As a result, see Fig. 5(a), the peak tensile σ_L^M at the weld center predicted using the TDCM is ~148 MPa (the green dash dot line), ~10 MPa higher than the prediction by the THDCM (the red solid line).

Fig. 5(a) shows that the effect of the THDCM on the L macroscopic RS σ_L^M beyond the shoulder edge is negligible since the heterogeneous thermal expansion and contraction are not significant and the plastic deformation is almost zero. Besides, Fig. 5(b) and (c) show that the T and N components of macroscopic RS, σ_T^M and σ_N^M , predicted based on the THDCM and the TDCM are almost the same. This agrees well with previous results [33,43,44].

Fig. 6(a), (b), (d) and (e) show that using the THDCM has some effect on the L and T components of the elastic mismatch RSes in both phases, i.e. $\sigma_L^{ma,eM}$, $\sigma_T^{ma,eM}$, $\sigma_L^{pa,eM}$ and $\sigma_T^{pa,eM}$, while this effect is negligible on $\sigma_N^{ma,eM}$ and $\sigma_N^{pa,eM}$, see Fig. 6(c) and (f). It can be seen that the THDCM has a small effect on the elastic mismatch RS, which is

consistent with that on the macroscopic RS. This is easy to understand because the elastic mismatch RS depends on the macroscopic RS linearly [10].

Fig. 7(a) and (b) show that the THDCM has considerable influence on the thermal misfit RS in both phases in the area near or within the shoulder edge, no matter whether the initial thermal misfit RS introduced in the previous quenching is considered or not. As shown in Fig. 7(a), with considering the initial thermal misfit RS, the peak thermal misfit RS in the matrix $\sigma^{ma,tM}$ predicted based on the TDCM is ~155 MPa and located at the weld center (the green dash dot line). Differently, the predicted peak $\sigma^{ma,tM}$ based on the THDCM is ~45 MPa lower and located near the outside of the shoulder edge (the red solid line). It is easy to understand the inverse profiles of $\sigma^{pa,tM}$ because of the relation

$$(1-V)\sigma^{ma,tM} + V\sigma^{pa,tM} = 0 \quad (7)$$

Summing up the M-m RSes, the total RSes predicted based on the THDCM and the TDCM are plotted in Fig. 8. Based on the THDCM, see the red solid line in Fig. 8(a), the predicted L total RS in the matrix $\sigma_L^{ma,total}$ has two peaks near the inside of the shoulder edge and have a tensile value of ~223 MPa, which is close to the experimental data. $\sigma_L^{ma,total}$ shows a platform of ~219 MPa between these two peaks. As expected, Fig. 8(a) and (d) show that the best predictions of $\sigma_L^{ma,total}$ and $\sigma_L^{pa,total}$ are based on the THDCM (the red solid line). Fig. 8(b) and (e) show that the predicted T total RSes $\sigma_T^{ma,total}$ and $\sigma_T^{pa,total}$ with no matter using the THDCM (the red solid line) or the TDCM (the green dash dot line) agree with the measured data in the BM reasonably, while they agree near or within the shoulder edge qualitatively. Fig. 8(c) shows that the predicted N total RS $\sigma_N^{ma,total}$ based on the THDCM or the TDCM is close to the measured data in the NZ, while it differs from the measured data significantly away from the NZ. Fig. 8(f) shows that the predicted N total RS $\sigma_N^{pa,total}$ based on the THDCM or the TDCM is close to the measured data in the BM, while it significantly differs from the measured data near or within the shoulder edge.

This work clearly shows that the THDCM improves the prediction of RSes in FSW MMCs, especially the accuracy of the thermal misfit and the

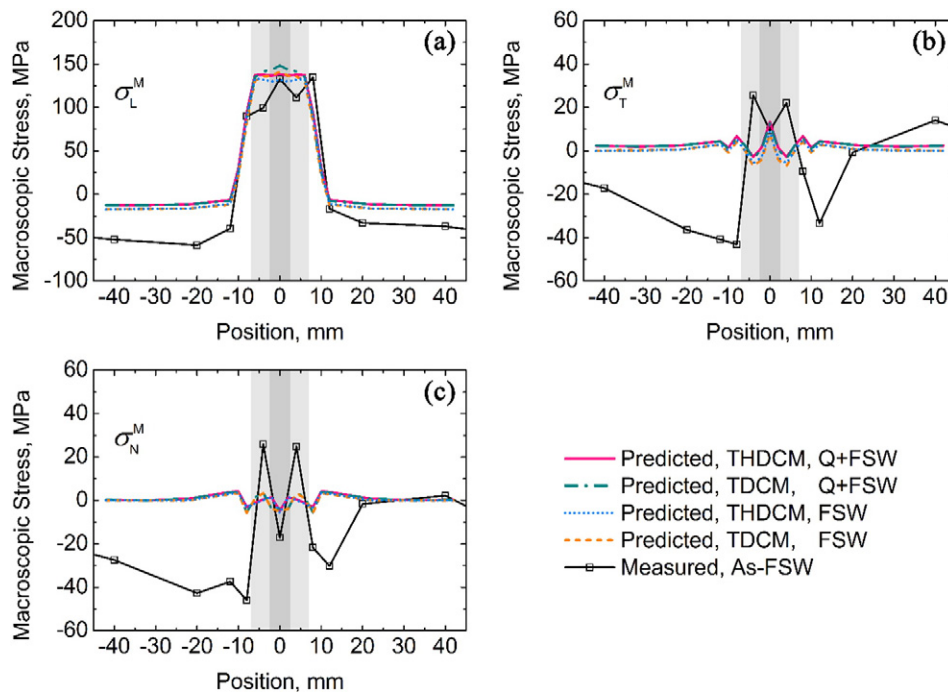


Fig. 5. Predicted macroscopic RS from different multiscale models and measured results for as-FSW sample. THDCM: temperature history dependent constitutive model; TDCM: temperature dependent constitutive model. The processes, which are taken into account, are denoted by FSW or Q + FSW (Q: Quenching).

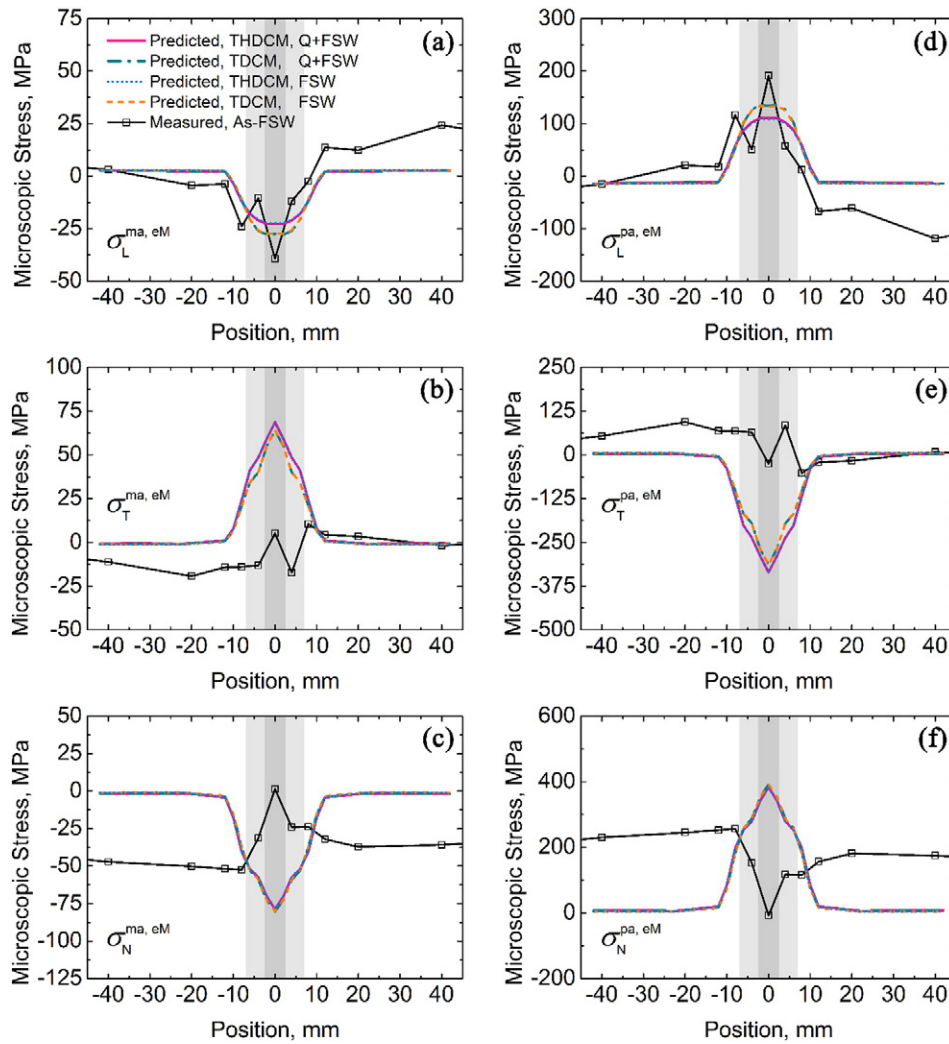


Fig. 6. Predicted elastic mismatch RS from different multiscale models and measured results for as-FSW sample. (The abbreviations in (a) have the same meanings with Fig. 5.)

total RSEs in the weld zone. If only the material softening effect at high temperature is considered by using the TDCM, then the predicted thermal misfit and the total RSEs are greatly overestimated in the weld zone.

5.4. Effects of initial RSEs from quenching before FSW

At the beginning, the FSW process of MMCs is modeled without considering any initial RS, like other macroscale models for welding of alloys usually behaves [33]. The results shown in Figs. 5 and 6 reveal that without considering any initial RS the predicted macroscopic and elastic mismatch RSEs reasonably agree with the measured data. Unfortunately, Fig. 7 shows that the traditional way of modeling welding RS without considering any initial RS failed to predict the thermal misfit RS in the BM, no matter using the TDCM (the yellow short dashed line) or the THDCM (the blue short dotted line). Although without considering initial RS the predicted thermal misfit RS $\sigma^{\beta,tm}$ based on the TDCM is close to the measured results in the NZ, it is usually believed that the values of $\sigma^{\beta,tm}$ predicted based on the TDCM are artificial and significantly overestimated.

To examine the predicted values of $\sigma^{\beta,tm}$ without considering initial RS, the effect of FSW thermal cycles is assessed. Fig. 9 shows the predicted $\sigma^{\beta,tm}$ without considering initial RS from previous quenching process versus the peak temperature. It shows that $\sigma^{\beta,tm}$ are near-zero for peak temperatures below $\sim 140^\circ\text{C}$, and their magnitudes increase faster and faster as the peak temperature increases from ~ 140

$\sim 266^\circ\text{C}$. Then above $\sim 266^\circ\text{C}$ the increase rate of $\sigma^{\beta,tm}$ slows down. This behavior is similar to the result of Dutta et al. [13], where the thermal misfit RS was first partially relaxed by plastic deformation and then regenerated by heat treatments. For instance, the regenerated $\sigma^{ma,tm}$ in a 22 vol.% SiCp/2124Al composite was ~ 50 MPa after heated to 180°C and ~ 64 MPa after heated to 300°C [13]. Therefore, the predicted near-zero $\sigma^{\beta,tm}$ in the BM is due to the low temperature. To overcome the wide gap in thermal misfit RS between the multiscale modeling and experiment, modification of the thermal model to rise up the peak temperature in the BM is not the right direction, because in the BM away from the weld zone the temperature should be low. Hence, other factor(s) should be taken into account.

The measured $\sigma^{ma,tm}$ and $\sigma^{pa,tm}$ in the BM are 70–90 MPa and $-332 \sim -438$ MPa, respectively. The order of these values fits the thermal misfit RSEs in the quenched 17 vol.% SiCp/Al composites, e.g. ~ 80 MPa [10], ~ 60 MPa [12,45] in the matrix; ~ -390 MPa [10], ~ -250 MPa [45] and ~ -280 MPa [12] in the particles. Therefore, the non-zero $\sigma^{\beta,tm}$ in the BM should be the thermal misfit RS mainly inherited from the previous quenching process before FSW. To verify this guess, both the previous quenching and the FSW processes are modeled.

Fig. 10 shows the macroscopic, elastic mismatch and thermal misfit RSEs in each phase resulting from the previous quenching. The predicted macroscopic RS is very small, ranging from 0 to ~ 5 MPa, in all the L, T and N directions. This is because the MMC plate is thin (thickness 3.1 mm). Since the elastic mismatch RS is the redistribution of the

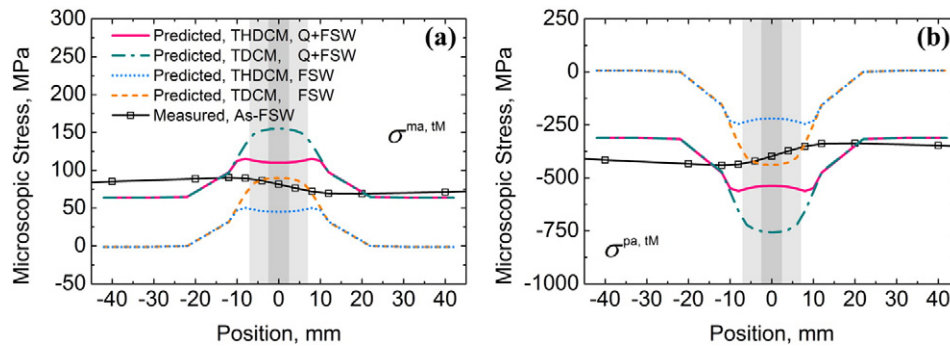


Fig. 7. Predicted thermal misfit RS from different multiscale models and measured results for as-FSW sample. (The abbreviations in (a) have the same meanings with Fig. 5.)

macroscopic RS between the two phases, it is easy to understand the near-zero elastic mismatch RS as shown in Fig. 10. The predicted thermal misfit RS resulting from the previous quenching is ~ 65 and ~ -318 MPa in the matrix and particles, respectively.

Then, these M-m RSEs resulting from the previous quenching were set as the corresponding initial RSEs in the FSW multiscale model. Fig. 5 shows that the macroscopic RS predicted with considering the initial macroscopic RS (the red solid and the green dash dotted lines) only have several MPa difference from those predicted without considering the initial macroscopic RS (the blue short dotted and the yellow short

dashed lines). Similarly, Fig. 6 shows that the predicted elastic mismatch RSEs with and without considering the initial elastic mismatch RS (induced by the previous quenching) slightly differ. The reason is that the initial macroscopic and elastic mismatch RSEs induced by the previous quenching are small in the present thin MMC plate.

For thick MMC (or alloy) plates, large RSEs can be produced during quenching [10,29,30,46,47], and these initial RSEs have to be taken into account to improve the accuracy for predicting M-m RSEs in the following thermo-mechanical process, e.g. FSW in this work. For instance, for a 75 mm thick 7449Al plate the macroscopic in-plane RS induced by

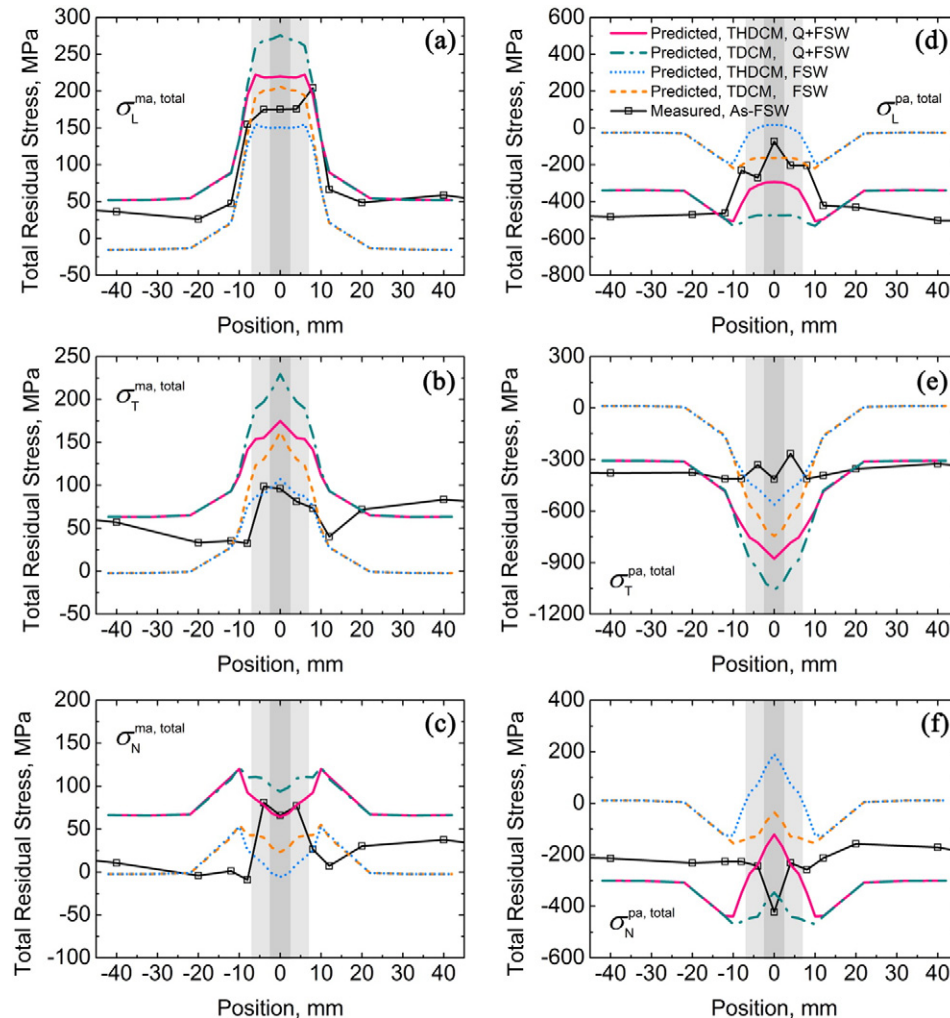


Fig. 8. Predicted total RS from different multiscale models and measured results for as-FSW sample. (The abbreviations in (d) have the same meanings with Fig. 5.)

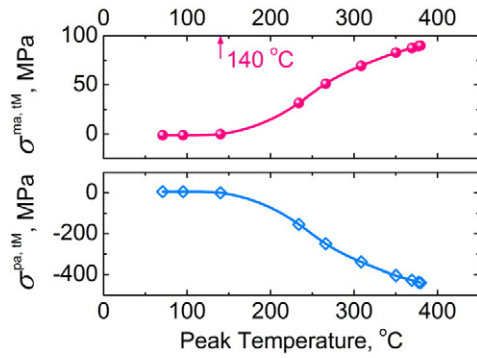


Fig. 9. Phase specific thermal misfit RS as function of experienced peak temperature. The results are predicted using TDCM without considering the initial RSes from the previous quenching.

quenching varies from ~ -300 MPa at surface to ~ 225 MPa at middle thickness [46]. For a 15 mm thick 17 vol.% SiCp/2124Al composite plate σ_t^M induced by quenching varies from ~ -150 MPa at surface to ~ 100 MPa at middle thickness, and $\sigma_t^{pa,eM}$ varies from ~ -50 MPa at surface to ~ 50 MPa in the middle [10,29,30].

Fig. 7 clarifies that with considering the initial thermal misfit RS the accuracy of the predicted thermal misfit RS after FSW is significantly

improved, no matter based on the THDCM or the TDCM. The modeling with considering the initial thermal misfit RS moves the predicted $\sigma^{ma,tm}$ or $\sigma^{pa,tm}$ line towards tensile or compressive by ~ 65 MPa or ~ -317 MPa, respectively. These results indicate that the initial thermal misfit RS does not change the basic profiles but approximately transfers the $\sigma^{ma,tm}$ or $\sigma^{pa,tm}$ after FSW by the value of the initial thermal misfit RS.

Fig. 8 shows that the effect of the initial RSes from the previous quenching on the total RS after FSW in each phase mainly follows that on the thermal misfit RS. By considering the initial M-m RSes (especially the initial thermal misfit RS), the accuracy of the predicted total RS can be greatly improved.

Figs. 7–8 reveal that to improve the accuracy of multiscale modeling of FSW MMC the initial thermal misfit RS must be taken into account. The initial M-m RSes generated in previous quenching approximately transfer the corresponding M-m RSes by the values of the initial RSes. For cases where the macroscopic and elastic mismatch RSes have large magnitudes, their effects on the RSes in the following process(es) must be taken into account.

5.5. Effects of post welding heat treatment

The experimental results plotted in Fig. 11 shows that the PWHT clearly changes the macroscopic RS. For instance, after PWHT, the

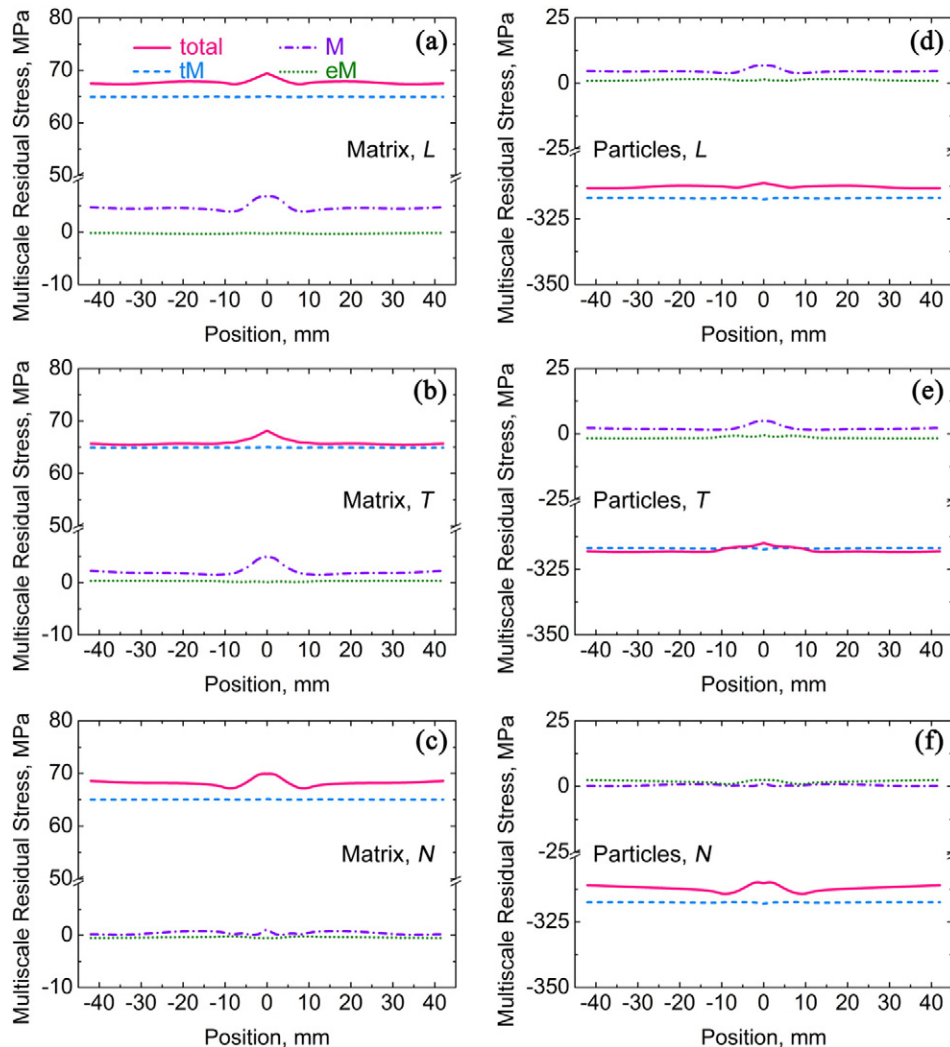


Fig. 10. The profiles of macroscopic (M), elastic mismatch (eM), thermal misfit (tM), and total RSes generated after previous quenching across all the macro-micro points. These RSes are then assigned as the initial macroscopic and microscopic RSes for the following FSW simulation.

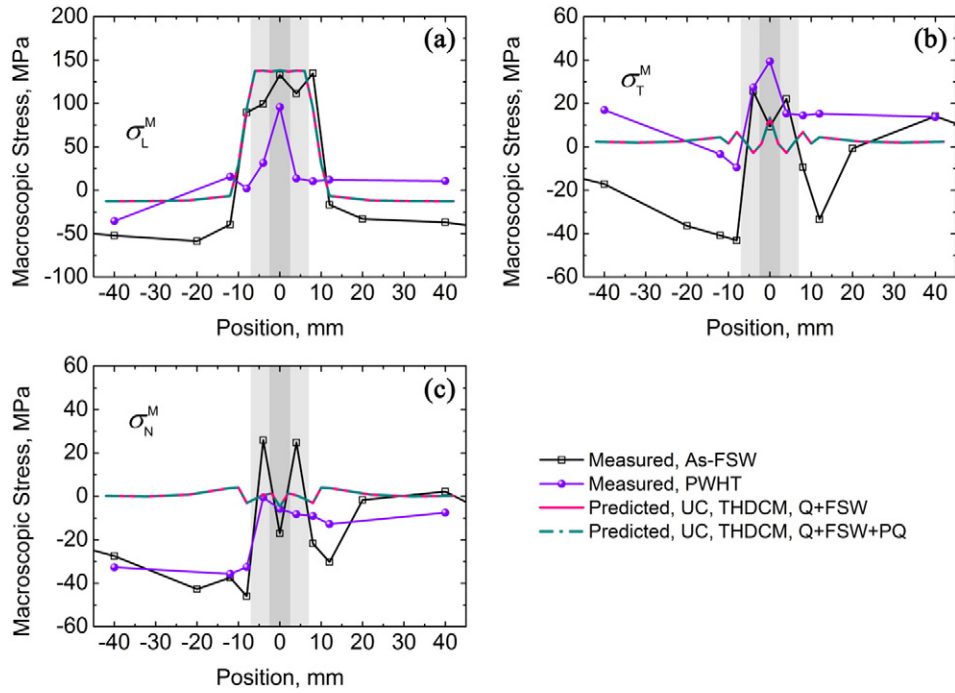


Fig. 11. Predicted macroscopic RS from different multiscale models and measured results for the As-FSW and PWHT samples. THDCM: temperature history dependent constitutive model; UC: unit cell; RVE5: RVE with size ratio of 5; Q + FSW: previous quenching and FSW are modeled; Q + FSW + PQ: previous quenching, FSW and post quenching are modeled.

magnitude of the measured σ_L^M in the BM decreases from ~ 50 MPa to near-zero, meanwhile, the width and the magnitude of the high tensile σ_L^M region decrease significantly. These experimental findings agree with the previous investigation [13], in which the macroscopic RS in a 22 vol.% SiCp/2124Al composite is continuously reduced with increasing the heat treatment time and temperature. However, Fig. 11 shows that σ_L^M , σ_T^M and σ_N^M predicted after PWHT almost have no variation compared with the those of the as-FSW state.

The experimental results plotted in Fig. 12(a) and (d) show that the PWHT decreases the widths of $\sigma_L^{ma,eM}$ and $\sigma_T^{pa,eM}$ profiles with high magnitudes. Meanwhile, after PWHT the profiles of $\sigma_L^{ma,eM}$ and $\sigma_T^{pa,eM}$ move to tension and compression, respectively. Fig. 12(b), (c), (e) and (f) show that the PWHT has small effects on the T and N components of the elastic mismatch RS. Especially in the weld zone the profiles and magnitudes of the measured $\sigma_T^{pa,eM}$, $\sigma_N^{ma,eM}$, $\sigma_T^{pa,eM}$ and $\sigma_N^{pa,eM}$ after PWHT have negligible variation compared with those of the as-FSW sample. However, Fig. 12 shows that the predicted elastic mismatch RS after PWHT has no variation compared with those of the as-FSW state.

Fig. 13(a) and (b) show that the measured thermal misfit RS in each phase after PWHT generally has the same level with that of the as-FSW state, while the predicted thermal misfit RS after PWHT has the same value as at the as-FSW state.

Fig. 14(a) shows that after PWHT the measured $\sigma_L^{ma,total}$ changes from ~ 50 to ~ 105 MPa in the BM, and the peak value decreases from ~ 204 to ~ 148 MPa. Nonetheless, Fig. 14(d) shows that after PWHT the measured $\sigma_L^{pa,total}$ keeps almost the same level in the BM, while the peak value decreases from around -74 to -160 MPa. Meanwhile, both the widths of measured $\sigma_L^{ma,total}$ and $\sigma_T^{pa,total}$ profiles with high values are significantly reduced. In the T and N directions the measured $\sigma_T^{ma,total}$, $\sigma_T^{pa,total}$, $\sigma_N^{ma,total}$ and $\sigma_N^{pa,total}$ after PWHT have small variations compared with the as-FSW state. However, in the modeling, Fig. 14 shows that after PWHT the predicted $\sigma_L^{\beta,total}$ has no variation compared with the as-FSW state.

Up to now the multiscale model cannot reproduce the reduction of RSes after PWHT. In order to illustrate the effect of the post quenching on the RSes, a virtual extreme post quenching (EPQ) process after previous quenching plus FSW processes was simulated. The coefficient of

heat convection in the EPQ was set as five times of that in the previous quenching. The RSes after virtual EPQ are plotted in Fig. 15. The EPQ process increases the level of macroscopic RS, and thereby the total RS. This agrees with the previous study [48], where the magnitudes of the macroscopic RS in a 7449Al alloy increase as the cooling rate of quenching rises. Nonetheless, Fig. 15 shows that the EPQ process has negligible effect on the elastic mismatch RS and no effect on the thermal misfit RS.

The PWHT is composed of three processes: solution treatment, quenching, and natural aging. Fig. 15 reveals that the post quenching process is not the reason for the reduction of the measured macroscopic, elastic mismatch and total RSes after PWHT, as shown in Figs. 11, 12 and 14. It is known that the natural aging process has small effects on the variations of RSes [49,50]. Therefore, in the three processes of PWHT, only the solution treatment can be the major possible factor causing the large reduction of the measured macroscopic, elastic mismatch and total RSes, especially in the NZ.

Many investigations reveal the influences of high temperature and preservation time on the RSes. For instance, in 8090Al-based MMC, over-aging treatment of 48 h at 190 °C reduced the compressive RS at surface from around 380 to 70 MPa [51]. In a 22 vol.% SiCp/2124Al composite, over-aging treatment of 48 h at 180 °C reduced the macroscopic RS by $\sim 70\%$ [13,52]. Furthermore, a simple empirical formula based on the Avrami relation, called the Zener-Wert-Avrami formula in references [53–55], is usually used to estimate the macroscopic stress relaxation due to thermally activated processes.

$$\frac{\sigma_t^{RS}}{\sigma_0^{RS}} = \exp \left[- \left(Bt \exp \left(- \frac{\Delta H}{kT} \right) \right)^m \right] \quad (8)$$

Most of the previous investigations using the Zener-Wert-Avrami formula focused on the 6xxx series Al alloys or corresponding composites. The parameters for these materials are summarized in Table 2.

According to Eq. (8), after solution treatment of 2 h at 505 °C the macroscopic RS at different locations should decrease with identical percentage. In fact, Fig. 11(a) shows that for σ_L^M the ratio between PWHT and as-FSW at position 0 mm is around 72% (96 MPa/133 MPa). However, this ratio at position 8 mm is around 7% (10 MPa/135 MPa).

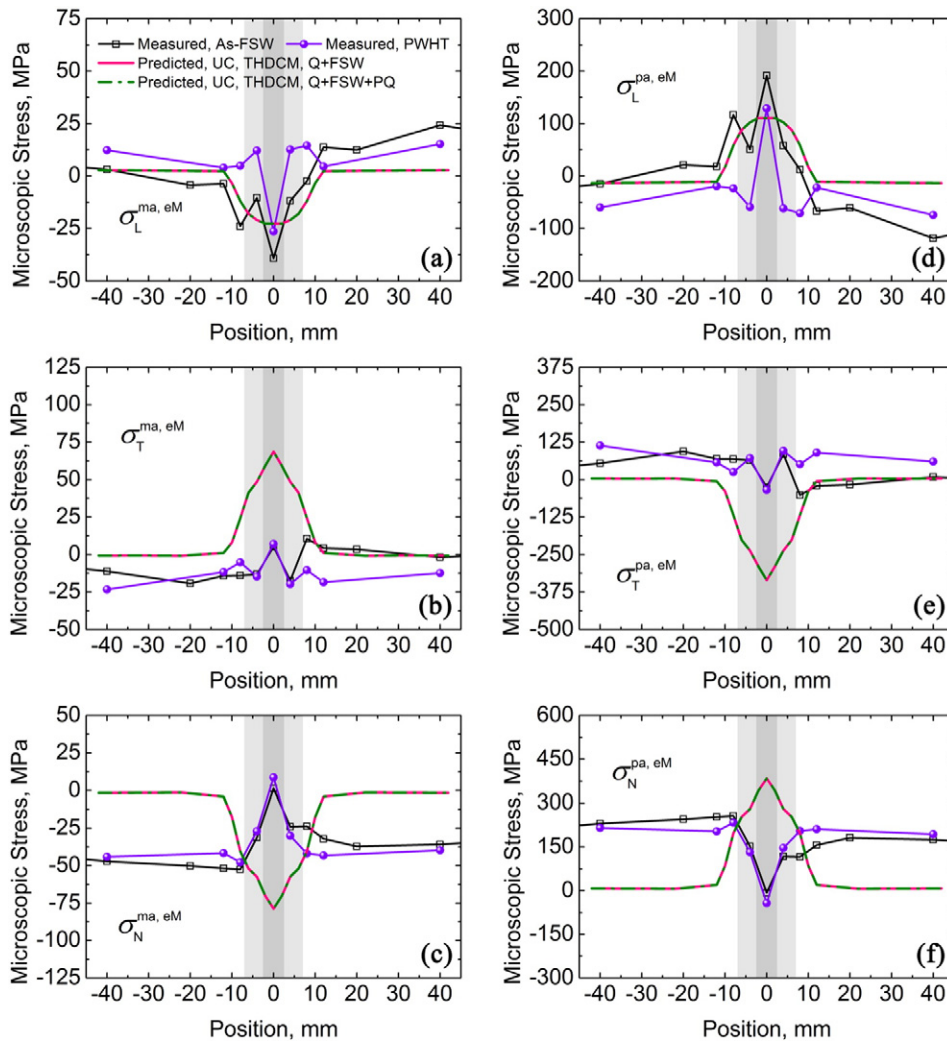


Fig. 12. Predicted elastic mismatch RS from different multiscale models and measured results for the As-FSW and PWHT samples. (The abbreviations in (a) have the same meanings with Fig. 11.)

This large disagreement indicates that in the FSW MMC joint the mechanism of macroscopic RS relaxation is much more complex and heterogeneous in different zones. The heterogeneous variations may be related to the unique heterogeneous microstructure of the FSW MMC joint. In [53–55] it is reported that materials having the same chemical composition but different precipitation states show different stress relaxation rates. In Al alloys, recrystallization probably occurs in severely deformed zones at relatively high temperatures for a short time, which leads to large reduction of RS and dislocation densities [54].

For FSW MMC, the presence of reinforcing particles (e.g. SiCp in this work) hinders the recrystallization process during solution treatment at 505 °C. During solution treatment at 505 °C, at least two mechanisms are responsible for stress relief. The first one is plastic deformation mechanism caused by the reduced yield stress at elevated temperature and the second one is creep mechanism [7]. The first mechanism occurs immediately as the temperature rises. This effect on the stress relaxation should be same for different zones as the temperature rises to 505 °C. The second mechanism dominates during the following period, and its effect on the stress relaxation varies at different zones of the weld [56].

5.6. Evolution of stresses during thermo-mechanical processes

Multiscale modeling can provide a rare look at the development of M-m RSes. Fig. 16 shows the evolution of the macroscopic stress along

the *L* direction with temperature at the macro-micro point P0. The initial stress at 516 °C of the previous quenching process is shown in Fig. 16 as point A. As the temperature decreases to room temperature at point B, point P0 is firstly compressed by the shrunk plate surface, and then it expands because the temperature at the plate core is higher than on the surface [29,30]. From point B to C, the FSW tool is getting closer and then reaches at the plate core, so it firstly is compressed by the area under the FSW tool that expands due to high temperature. When point P0 is under the FSW tool, it expands gradually until the peak temperature is reached. Plastic deformation occurs to maintain geometrical compatibility when the FSW tool is close to and above point P0. As the FSW tool passes away, the temperature decreases at point P0, thereby it is stretched by the part in the BM [7]. When the temperature decreases to room temperature, all the constraints like jigs on the MMC plate are removed and the macroscopic RS maintains (point D).

The macroscopic stress varies linearly as the MMC plate is raised to solution temperature 505 °C (point E), as shown in Fig. 16. In the present multiscale models, the stress relaxation stage is not taken into account, so only stress redistribution occurs at solution temperature. As the temperature decreases to room temperature, the curve EF mimics the profile of curve AB. Point F is nearly the same as point D, which reveals negligible plastic deformation during the post quenching process.

Fig. 17(a) and (d) show the complex evolution of elastic mismatch stress, which represents the extent of load transfer of the macroscopic

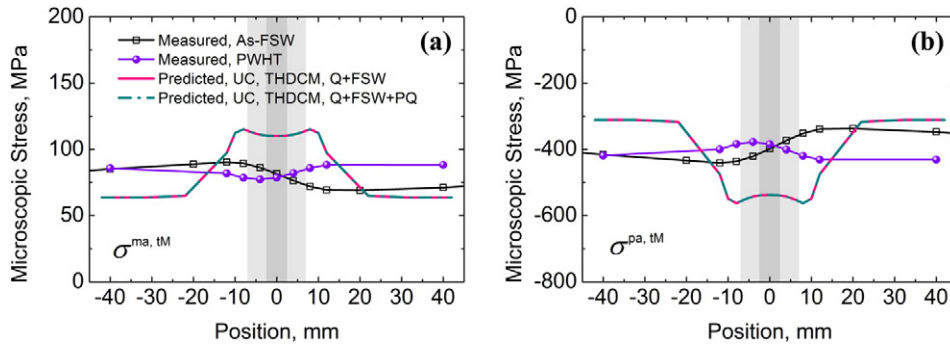


Fig. 13. Predicted thermal misfit RS from different multiscale models and measured results for as-FSW and PWHT samples. (The abbreviations in (a) have the same meanings with Fig. 11.)

stress from the matrix to the particles. The magnitude of the elastic mismatch stress depends on the shape and volume fraction of the particles as well as the elastic properties of the two phases [10]. As expected, the profiles of $\sigma_L^{ma,eM}$ and $\sigma_T^{pa,eM}$ are opposite. The increase of magnitude before point D is caused by the release of all constraints after FSW.

Fig. 17(b) and (e) show the evolution of thermal misfit stress from previous quenching temperature A to room temperature B. The nonlinearity of curve AB is mainly caused by the plastic deformation [29,30]. At the beginning of the FSW process, the matrix expands and the tensile $\sigma^{ma,tm}$ reduces linearly as the temperature raises. When the temperature is higher than $\sim 140^\circ\text{C}$, the thermal misfit is large enough, plastic

deformation occurs, thereby, $\sigma^{ma,tm}$ varies nonlinearly. The turn of curve BC in Fig. 17(b) or (e) is caused by plastic deformation in the matrix, which starts at $\sim 140^\circ\text{C}$. As the FSW tool passes away, temperature decreases, the matrix contracts, and it is constrained by the ceramic particles. Hence, $\sigma^{ma,tm}$ increases to tension. As expected, the profiles of $\sigma^{ma,tm}$ and $\sigma^{pa,tm}$ are opposite.

The predicted evolution of thermal misfit stress during the FSW thermal cycle in this work probably clarifies that the guessed evolution curve of thermal misfit stress during aging was wrong in [13]. The guess showed that the thermal misfit stress evolved linearly with the temperature rising from room temperature to aging temperature ($\geq 180^\circ\text{C}$)

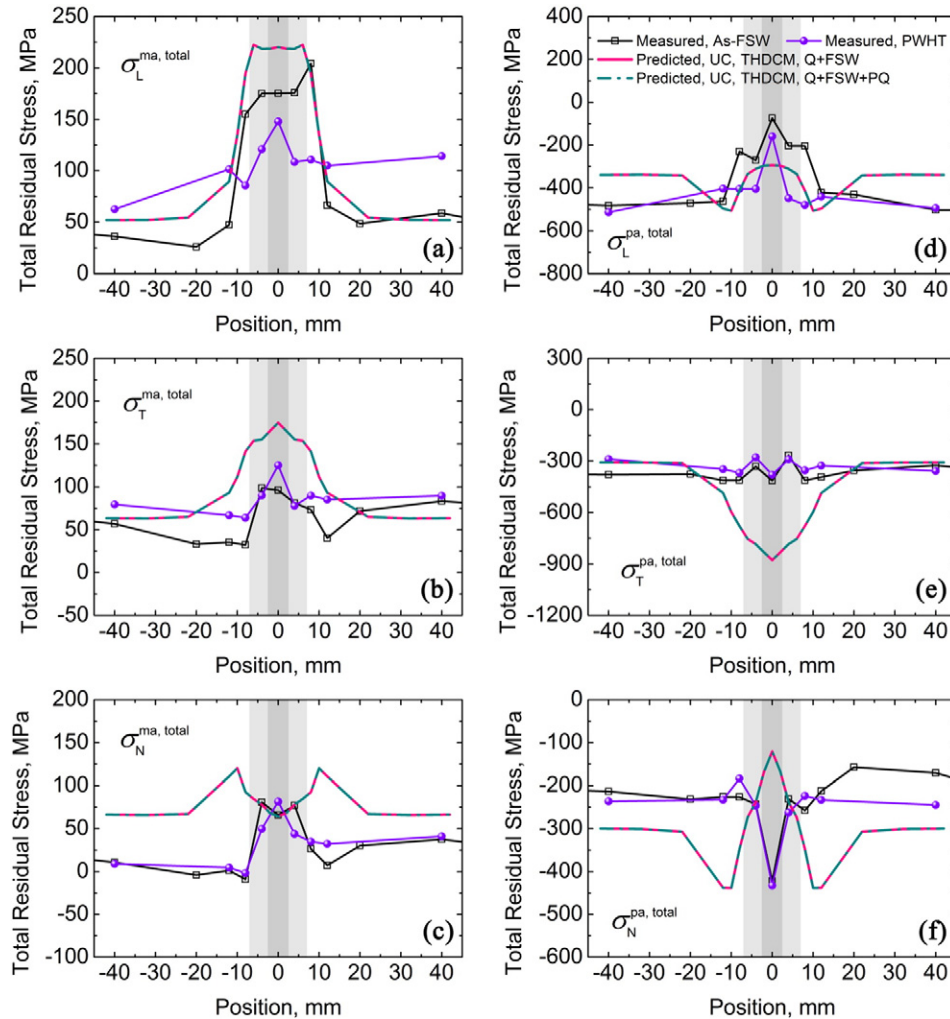


Fig. 14. Predicted total RS from different multiscale models and measured results for as-FSW and PWHT samples. (The abbreviations in (d) have the same meanings with Fig. 11.)

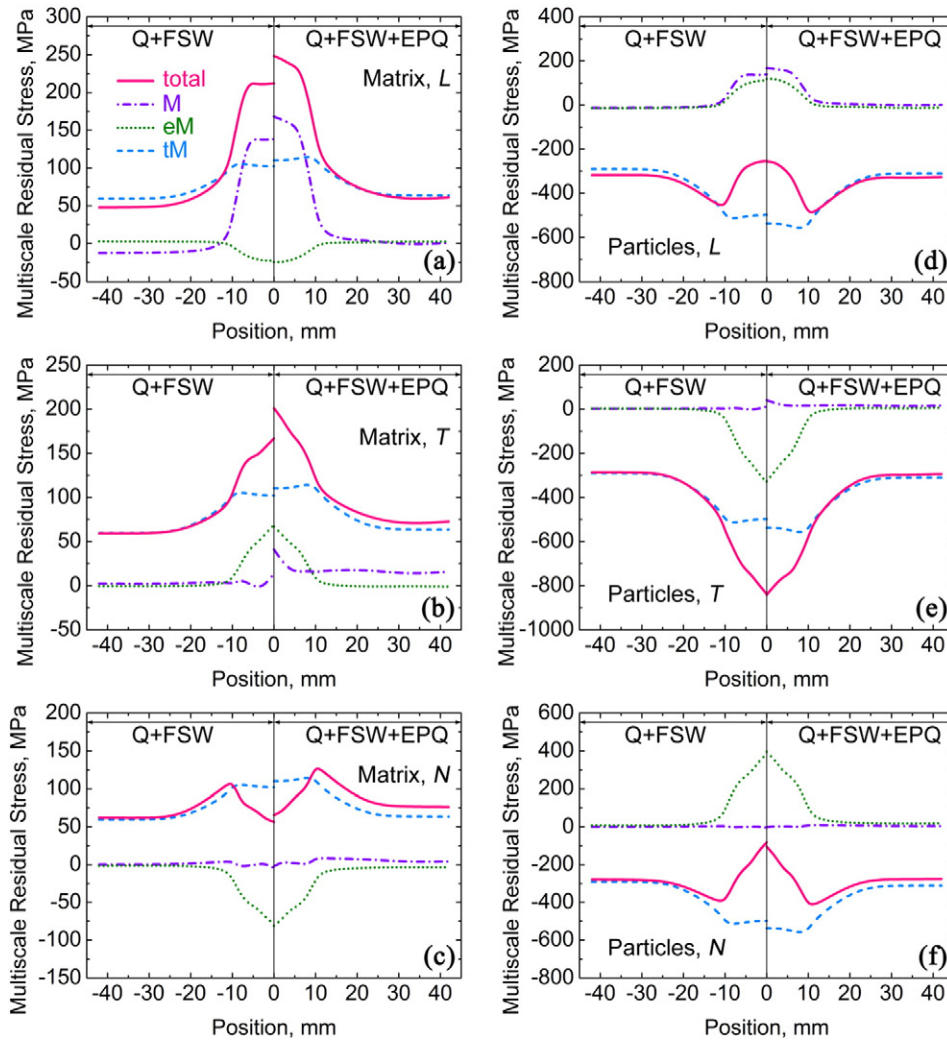


Fig. 15. Comparison of the macroscopic and microscopic RSes across all the macro-micro points between the Q + FSW and the Q + FSW + EPQ multiscale models. EPQ: virtual extreme post quenching.

[13]. The present work shows that when the temperature is higher than ~140 °C, plastic deformation occurs due to large thermal misfit. As plastic deformation is present, the evolution of thermal misfit stress is not linear anymore. Such nonlinear evolution of thermal misfit stress with the temperature has been experimentally observed in [9,57].

Integrating all the M-m stresses, the evolution of total stresses in both phases are plotted in Fig. 17(c) and (f). The evolution curves of $\sigma_L^{ma, total}$ and $\sigma_L^{pa, total}$ from point A to F are very different and not opposite. Note that if the stress relaxation stage is considered during solution treatment, there will be a drop from point E to point E' as virtually plotted in Fig. 17(c) and (f). The final stress state will move to point F'. Such a drop is mainly caused by the reduction of macroscopic and elastic mismatch RSes. In contrast, the thermal misfit RS will maintain its

magnitude after PWHT, because it mainly depends on the temperature drop and the difference of CTE between the two phases.

5.7. Accuracy of the multiscale modeling and the neutron diffraction measurements

Fig. 6(b), (c), (e) and (f), Fig. 12(b), (c), (e) and (f), and Fig. 13 show that there are big differences between the measurements and simulations for some microscopic RS components, i.e. the T and N components of the elastic mismatch RS and the thermal misfit RS. These differences are the major reason that causing the big differences between the measurements and simulations for the T and N components of the total RS as shown in Fig. 8(b), (c), (e) and (f), and Fig. 14(b), (c), (e) and (f). The reasons for these errors probably come from several aspects, as discussed in the following.

As shown in previous studies [29,30,35], several main aspects affect the accuracy of multiscale modeling. In this work, the finite element mesh of UC is non-periodic. Hence, the KUBC was adopted as the macro-micro transition BC for computing the elastic mismatch and thermal misfit RSes. The KUBC predicts upper bounds of the target properties [30]. These bounds converge to the correct value as the domain size of the microscale model increases. Applying large representative volume elements can gain the advantage of high accuracy, but suffers from high computational cost.

Table 2
Constants of Zener-Wert-Avrami function for various materials.

Material	m	ΔH , eV	B, min ⁻¹	Reference
6110Al-T6	0.22	1.35	3.06E12	[53]
As-quenched 6110Al	0.17	1.63	4.59E16	[54]
Under-aged 6110Al	0.21	1.51	4.42E13	[55]
6061Al-T651	0.22	1.35	3.06E12	[62]
10 vol.% SiCw/6061Al-T6	0.20	1.40	1.50E12	[63]
10 vol.% TiB ₂ /6351Al	0.24	1.64	3.90E13	[64]

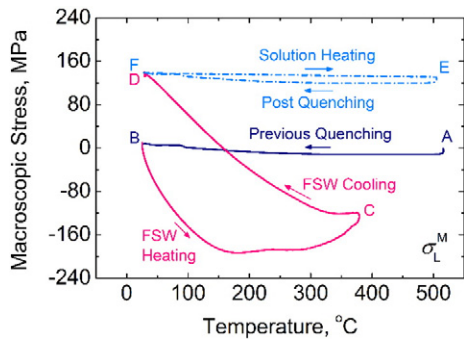


Fig. 16. Evolution of macroscopic stress during the complete thermal cycle from previous quenching (AB), to FSW (BCD) and to post quenching (DEF).

Complex physical phenomena are usually involved in multi-thermo-mechanical processes. Modeling the detailed physical processes to predict M-m RSes accurately is almost impossible at present. A practical and efficient way is to develop a reduced model. In this work, the quenching process was modeled by taking into account the temperature dependent material properties and the thermal contact to the quenching medium. The FSW process was modeled based on appropriate empirical constitutive model, i.e. the THDCM, which can reflect the

precipitation and dislocation density variations, dynamic recrystallization and material softening [33,43,44]. The intense material flow, particle cracking and rotation/redistribution, newly formed cleaner and stronger particle/matrix interfaces in the NZ, and newly formed nanometer sized Al grains on or near the particle/matrix interfaces in the NZ were not considered during FSW, because it is too complex to consider these factors.

Besides, in this work, the multiscale model does not consider the natural aging processes. These processes have small effects on the RS relaxation, however, they are not the major processes. Such simplification introduces small, yet acceptable errors in principle. Other aspects affecting the accuracy of multiscale modeling include the input data for the model such as coefficient of heat convection, material properties at different temperatures and temperature histories, boundary conditions at the macroscale model [58].

Concerning the neutron diffraction measurements, in the project “European Network on Neutron Techniques standardization for Structural Integrity”, five different laboratories with different neutron diffraction instruments independently measured the RS in a single weld bead on a plate specimen [59]. The investigations revealed that in the region away from the weld the best measurements have ± 23 MPa systematic errors and ± 47 MPa random errors. In the weld zone the best measurements have ± 47 MPa systematic errors and ± 47 MPa random errors. Many factors can influence the accuracy of neutron

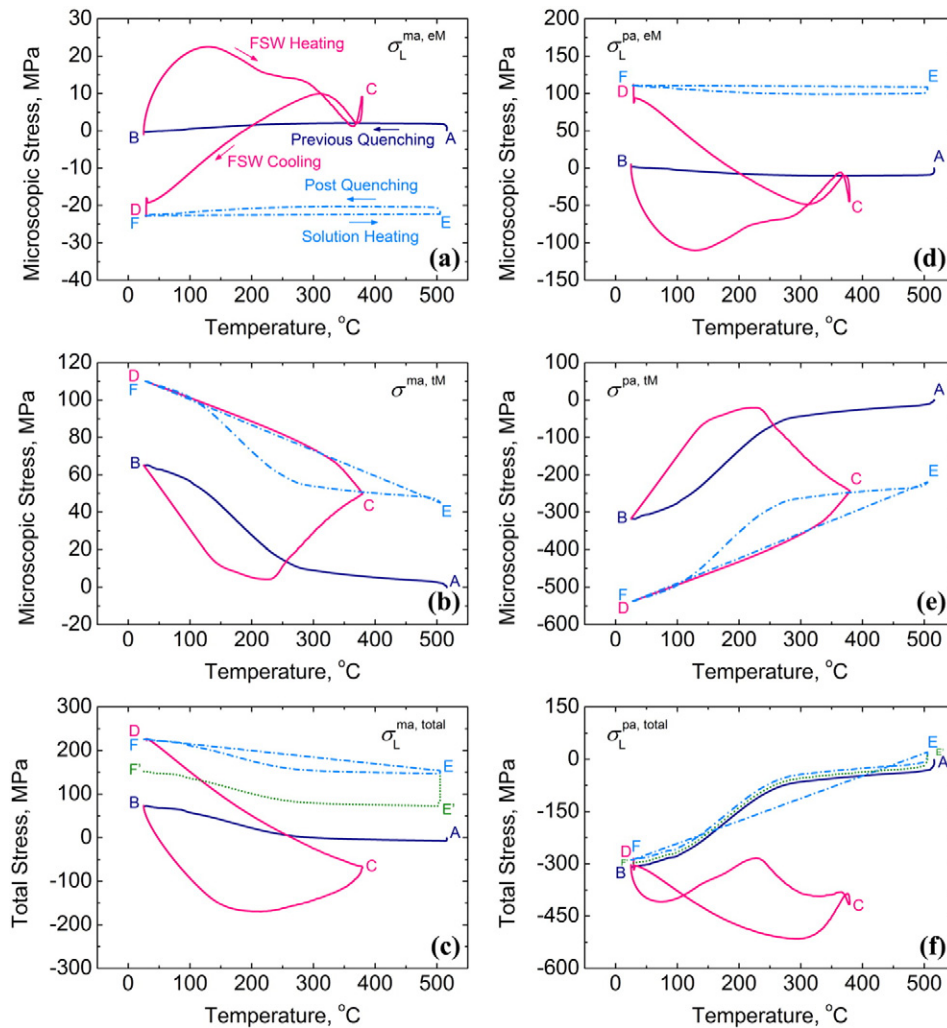


Fig. 17. Evolution of elastic mismatch ((a), (d)), thermal misfit ((b), (e)) and total ((c), (f)) stresses during the complete thermal cycle from previous quenching (AB), to FSW (BCD) and to post quenching (DEF) at macro-micro point P0. The results are predicted from the multiscale model based on UC, THDCM and Q + FSW + PQ. In (c) and (f) the effect of stress relaxation due to solution treatment is illustrated by EE'F'.

diffraction measurements [59], which include lattice parameters of unstrained reference [10,59], diffraction elastic constants [59], crystallographic texture [59–61] and grain size [59]. Therefore, accurate determination of RSEs in FSW MMCs requires a measurement system analysis. However, such an analysis would demand a lot of beam time and is very costly.

6. Conclusions

An enhanced hierarchical multiscale model has been developed in conjunction with neutron diffraction to rationalize the observations of M-m RSEs in MMCs during multi-thermo-mechanical processes. As an example, the M-m RSEs in the 17 vol.% SiCp/2009Al-T4 plates during previous quenching, FSW and PWHT were investigated. The conclusions can be summarized as follows:

- (1) The THDCM improves the prediction of RSEs in FSW MMCs, especially the thermal misfit and the total RSEs in the weld zone. The predicted thermal misfit and total RSEs based on TDCM are greatly overestimated in the weld zone. The macroscopic and elastic mismatch RSEs predicted based on the THDCM and the TDCM have small difference. For improving the accuracy of predictions for the welding process, we recommend the THDCM.
- (2) By considering the initial thermal misfit RS from previous quenching, the accuracy of the predicted thermal misfit and total RSEs after FSW is significantly improved, no matter based on the THDCM or the TDCM. The macroscopic and elastic mismatch RSEs from previous quenching are small due to the thin thickness of the MMC plate, which result in small effects on the macroscopic and elastic mismatch RSEs after FSW.
- (3) The reduction of macroscopic, elastic mismatch and the total RSEs during PWHT in the experiment is mainly caused by the stress relaxation during solution treatment stage; but not during the post quenching stage, which tend to increase the RS level.

Acknowledgments

The authors gratefully acknowledge support from the National Natural Science Foundation of China [Grant No. 51401219] and the National Basic Research Program of China [Grant No. 2012CB619600]. The authors are very grateful to the staff of FRM II Garching, Germany, for their kind support of the experiments.

References

- [1] A.P. Reynolds, W. Tang, T. Gnaupel-Herold, H. Prask, Structure, properties, and residual stress of 304L stainless steel friction stir welds, *Scr. Mater.* 48 (2003) 1289–1294.
- [2] S. Sadeghi, M.A. Najafabadi, Y. Javadi, M. Mohammadisefat, Using ultrasonic waves and finite element method to evaluate through-thickness residual stresses distribution in the friction stir welding of aluminum plates, *Mater. Des.* 52 (2013) 870–880.
- [3] A.R. Darvazi, M. Iranmanesh, Prediction of asymmetric transient temperature and longitudinal residual stress in friction stir welding of 304L stainless steel, *Mater. Des.* 55 (2014) 812–820.
- [4] H. Jamshidi Aval, Microstructure and residual stress distributions in friction stir welding of dissimilar aluminium alloys, *Mater. Des.* 87 (2015) 405–413.
- [5] J.W. Sowards, T. Gnaupel-Herold, J.D. McColskey, V.F. Pereira, A.J. Ramirez, Characterization of mechanical properties, fatigue-crack propagation, and residual stresses in a microalloyed pipeline-steel friction-stir weld, *Mater. Des.* 88 (2015) 632–642.
- [6] M.E. Kassner, P. Geantil, L.E. Levine, Long range internal stresses in single-phase crystalline materials, *Int. J. Plast.* 45 (2013) 44–60.
- [7] P.J. Withers, Residual stress and its role in failure, *Rep. Prog. Phys.* 70 (2007) 2211–2264.
- [8] M. Koc, J. Culp, T. Altan, Prediction of residual stresses in quenched aluminum blocks and their reduction through cold working processes, *J. Mater. Process. Technol.* 174 (2006) 342–354.
- [9] M. Schoebel, G. Baumgartner, S. Gerth, J. Bernardi, M. Hofmann, Microstresses and crack formation in AlSi7MgCu and AlSi17Cu4 alloys for engine components, *Acta Mater.* 81 (2014) 401–408.
- [10] M.E. Fitzpatrick, M.T. Hutchings, P.J. Withers, Separation of macroscopic, elastic mismatch and thermal expansion misfit stresses in metal matrix composite quenched plates from neutron diffraction measurements, *Acta Mater.* 45 (1997) 4867–4876.
- [11] X.X. Zhang, D.R. Ni, B.L. Xiao, H. Andrae, W.M. Gan, M. Hofmann, Z.Y. Ma, Determination of macroscopic and microscopic residual stresses in friction stir welded metal matrix composites via neutron diffraction, *Acta Mater.* 87 (2015) 161–173.
- [12] M.E. Fitzpatrick, P.J. Withers, A. Baczmanski, M.T. Hutchings, R. Levy, M. Ceretti, A. Lodini, Changes in the misfit stresses in an Al/SiC_p metal matrix composite under plastic strain, *Acta Mater.* 50 (2002) 1031–1040.
- [13] M. Dutta, G. Bruno, L. Edwards, M.E. Fitzpatrick, Neutron diffraction measurement of the internal stresses following heat treatment of a plastically deformed Al/SiC particulate metal-matrix composite, *Acta Mater.* 52 (2004) 3881–3888.
- [14] P. Fernandez-Castrillo, G. Bruno, G. Gonzalez-Doncel, Neutron and synchrotron radiation diffraction study of the matrix residual stress evolution with plastic deformation in aluminum alloys and composites, *Mat. Sci. Eng. A* 487 (2008) 26–32.
- [15] M. Schoebel, H.P. Degischer, S. Vaucher, M. Hofmann, P. Cloetens, Reinforcement architectures and thermal fatigue in diamond particle-reinforced aluminum, *Acta Mater.* 58 (2010) 6421–6430.
- [16] M. Schoebel, W. Altendorfer, H.P. Degischer, S. Vaucher, T. Buslaps, M. Di Michiel, M. Hofmann, Internal stresses and voids in SiC particle reinforced aluminum composites for heat sink applications, *Compos. Sci. Technol.* 71 (2011) 724–733.
- [17] J.D. Eshelby, The determination of the elastic field of an ellipsoidal inclusion, and related problems, *Proc. R Soc. Lon. Ser-A* 241 (1957) 376–396.
- [18] P.J. Withers, W.M. Stobbs, O.B. Pedersen, The application of the Eshelby method of internal-stress determination to short fiber metal matrix composites, *Acta Metall.* 37 (1989) 3061–3084.
- [19] G.L. Povirk, M.G. Stout, M. Bourke, J.A. Goldstone, A.C. Lawson, M. Lovato, S. Macewen, S. Nutt, A. Needleman, Thermally and mechanically induced residual strains in Al-SiC composites, *Acta Metall. Mater.* 40 (1992) 2391–2412.
- [20] M. Sauerborn, H.J. McQueen, Modelling extrusion of 2618 aluminium alloy and 2618-10%Al₂O₃ and 2618-20%Al₂O₃ composites, *Mater. Sci. Technol.* 14 (1998) 1029–1038.
- [21] D. Golanski, K. Terada, N. Kikuchi, Macro and micro scale modeling of thermal residual stresses in metal matrix composite surface layers by the homogenization method, *Comput. Mech.* 19 (1997) 188–202.
- [22] F. Feyel, Multiscale FE² elastoviscoplastic analysis of composite structures, *Comput. Mater. Sci.* 16 (1999) 344–354.
- [23] I. Doghri, A. Ouair, Homogenization of two-phase elasto-plastic composite materials and structures - study of tangent operators, cyclic plasticity and numerical algorithms, *Int. J. Solids Struct.* 40 (2003) 1681–1712.
- [24] P. Kanoute, D.P. Boso, J.L. Chaboche, B.A. Schrefler, Multiscale methods for composites: a review, *Arch. Comput. Method Eng.* 16 (2009) 31–75.
- [25] J. Llorca, C. Gonzalez, J.M. Molina-Aldareguia, J. Segurado, R. Seltzer, F. Sket, M. Rodriguez, S. Sadaba, R. Munoz, L.P. Canal, Multiscale modeling of composite materials: a roadmap towards virtual testing, *Adv. Mater.* 23 (2011) 5130–5147.
- [26] J. Spahn, H. Andrae, M. Kabel, R. Mueller, A multiscale approach for modeling progressive damage of composite materials using fast Fourier transforms, *Comput. Method Appl. M* 268 (2014) 871–883.
- [27] E. Weinan, B. Engquist, X.T. Li, W.Q. Ren, E. Vanden-Eijnden, Heterogeneous multiscale methods: a review, *Commun. Comput. Phys.* 2 (2007) 367–450.
- [28] T. Belytschko, J.H. Song, Coarse-graining of multiscale crack propagation, *Int. J. Numer. Methods Eng.* 81 (2010) 537–563.
- [29] X.X. Zhang, B.L. Xiao, H. Andrae, Z.Y. Ma, Multi-scale modeling of the macroscopic, elastic mismatch and thermal misfit stresses in metal matrix composites, *Compos. Struct.* 125 (2015) 176–187.
- [30] X.X. Zhang, B.L. Xiao, H. Andrae, Z.Y. Ma, Multiscale modeling of macroscopic and microscopic residual stresses in metal matrix composites using 3D realistic digital microstructure models, *Compos. Struct.* 137 (2016) 18–32.
- [31] X.X. Zhang, B.L. Xiao, Z.Y. Ma, A transient thermal model for friction stir weld. Part I: the model, *Metall. Mater. Trans. A* 42A (2011) 3218–3228.
- [32] X.X. Zhang, B.L. Xiao, Z.Y. Ma, A transient thermal model for friction stir weld. Part II: effects of weld conditions, *Metall. Mater. Trans. A* 42A (2011) 3229–3239.
- [33] R.V. Preston, H.R. Shercliff, P.J. Withers, S. Smith, Physically-based constitutive modelling of residual stress development in welding of aluminium alloy 2024, *Acta Mater.* 52 (2004) 4973–4983.
- [34] X.X. Zhang, Q. Zhang, T. Zangmeister, B.L. Xiao, H. Andrae, Z.Y. Ma, A three-dimensional realistic microstructure model of particle-reinforced metal matrix composites, *Model. Simul. Mater. Sci. Eng.* 22 (2014) 035010 (21pp).
- [35] X.X. Zhang, B.L. Xiao, H. Andrae, Z.Y. Ma, Homogenization of the average thermo-elastoplastic properties of particle reinforced metal matrix composites: the minimum representative volume element size, *Compos. Struct.* 113 (2014) 459–468.
- [36] E. Voce, A practical strain-hardening function, *Metallurgica* 51 (1955) 219–226.
- [37] D. Wang, Q.Z. Wang, B.L. Xiao, Z.Y. Ma, Achieving friction stir welded SiCp/Al-Cu-Mg composite joint of nearly equal strength to base material at high welding speed, *Mat Sci Eng A* 589 (2014) 271–274.
- [38] D. Wang, B.L. Xiao, Q.Z. Wang, Z.Y. Ma, Evolution of the microstructure and strength in the nugget zone of friction stir welded SiCp/Al-Cu-Mg composite, *J. Mater. Sci. Technol.* 30 (2014) 54–60.
- [39] D.R. Ni, D.L. Chen, B.L. Xiao, D. Wang, Z.Y. Ma, Residual stresses and high cycle fatigue properties of friction stir welded SiCp/AA2009 composites, *Int. J. Fatigue* 55 (2013) 64–73.
- [40] D.R. Ni, D.L. Chen, D. Wang, B.L. Xiao, Z.Y. Ma, Tensile properties and strain-hardening behaviour of friction stir welded SiCp/AA2009 composite joints, *Mat Sci Eng A* 608 (2014) 1–10.
- [41] A. Simar, Y. Brechet, B. de Meester, A. Denquin, T. Pardoen, Sequential modeling of local precipitation, strength and strain hardening in friction stir welds of an aluminium alloy 6005A-T6, *Acta Mater.* 55 (2007) 6133–6143.

- [42] A. Simar, Y. Brechet, B. de Meester, A. Denquin, C. Gallais, T. Pardoen, Integrated modeling of friction stir welding of 6xxx series Al alloys: process, microstructure and properties, *Prog. Mater. Sci.* 57 (2012) 95–183.
- [43] Z.L. Zhang, J. Silvanus, H.K. Li, Q.Y. Shi, Sensitivity analysis of history dependent material mechanical models for numerical simulation of welding process, *Sci. Technol. Weld. Join.* 13 (2008) 422–429.
- [44] D.Y. Yan, A.P. Wu, J. Silvanus, Q.Y. Shi, Predicting residual distortion of aluminum alloy stiffened sheet after friction stir welding by numerical simulation, *Mater. Des.* 32 (2011) 2284–2291.
- [45] M.E. Fitzpatrick, M.T. Hutchings, P.J. Withers, Separation of measured fatigue crack stress fields in a metal matrix composite material, *Acta Mater.* 47 (1999) 585–593.
- [46] N. Chobaut, D. Carron, S. Arsene, P. Schloth, J.M. Drezet, Quench induced residual stress prediction in heat treatable 7xxx aluminium alloy thick plates using Gleeble interrupted quench tests, *J. Mater. Process. Technol.* 222 (2015) 373–380.
- [47] M.B. Prime, M.R. Hill, Residual stress, stress relief, and inhomogeneity in aluminum plate, *Scr. Mater.* 46 (2002) 77–82.
- [48] J.S. Robinson, D.A. Tanner, S. van Petegem, A. Evans, Influence of quenching and aging on residual stress in Al-Zn-Mg-Cu alloy 7449, *Mater. Sci. Technol.* 28 (2012) 420–430.
- [49] V.M. Linton, M.I. Ripley, Influence of time on residual stresses in friction stir welds in agehardenable 7xxx aluminium alloys, *Acta Mater.* 56 (2008) 4319–4327.
- [50] W. Woo, Z. Feng, X.L. Wang, C.R. Hubbard, Neutron diffraction measurements of time-dependent residual stresses generated by severe thermomechanical deformation, *Scr. Mater.* 61 (2009) 624–627.
- [51] D.M. Knowles, J.E. King, Influence of macroscopic residual-stress fields on fatigue crack-growth measurement in sic particulate reinforced 8090 aluminum-alloy, *Mater. Sci. Technol.* 7 (1991) 1015–1020.
- [52] M.E. Fitzpatrick, M.T. Hutchings, J.E. King, D.M. Knowles, P.J. Withers, Effect of thermal residual stresses on fatigue crack opening and propagation behavior in an Al/SiC_p metal matrix composite, *Metall. Mater. Trans. A* 26 (1995) 3191–3198.
- [53] P. Juijerm, I. Altenberger, Residual stress relaxation of deep-rolled Al-Mg-Si-Cu alloy during cyclic loading at elevated temperatures, *Scr. Mater.* 55 (2006) 1111–1114.
- [54] P. Juijerm, I. Altenberger, B. Scholtes, Influence of ageing on cyclic deformation behavior and residual stress relaxation of deep rolled as-quenched aluminium alloy AA6110, *Int. J. Fatigue* 29 (2007) 1374–1382.
- [55] P. Juijerm, I. Altenberger, Effect of temperature on cyclic deformation behavior and residual stress relaxation of deep rolled under-aged aluminium alloy AA6110, *Mat Sci Eng A* 452 (2007) 475–482.
- [56] Z.Y. Ma, S.C. Tjong, Creep deformation characteristics of discontinuously reinforced aluminium-matrix composites, *Compos. Sci. Technol.* 61 (2001) 771–786.
- [57] G. Requena, D.C. Yubero, J. Corrochano, J. Repper, G. Garces, Stress relaxation during thermal cycling of particle reinforced aluminium matrix composites, *Compos. Pt. A* 43 (2012) 1981–1988.
- [58] X.K. Zhu, Y.J. Chao, Effects of temperature-dependent material properties on welding simulation, *Comput. Struct.* 80 (2002) 967–976.
- [59] R.C. Wimpory, C. Ohms, M. Hofmann, R. Schneider, A.G. Youtsos, Statistical analysis of residual stress determinations using neutron diffraction, *Int. J. Press. Vessel. Pip.* 86 (2009) 48–62.
- [60] J.M. Root, D.P. Field, T.W. Nelson, Crystallographic texture in the friction-stir-welded metal matrix composite Al6061 with 10 vol pct Al₂O₃, *Metall. Mater. Trans. A* 40A (2009) 2109–2114.
- [61] J. Guo, S. Amira, P. Gougeon, X.G. Chen, Effect of the surface preparation techniques on the EBSD analysis of a friction stir welded AA1100-B4C metal matrix composite, *Mater. Charact.* 62 (2011) 865–877.
- [62] X.D. Ren, L. Ruan, S.Q. Yuan, H.M. Yang, Q.B. Zhan, L.M. Zheng, Y. Wang, F.Z. Dai, Metallographic structure evolution of 6061-T651 aluminum alloy processed by laser shock peening: effect of tempering at the elevated temperatures, *Surf. Coat. Technol.* 221 (2013) 111–117.
- [63] J. Huang, Z. Wang, K. Bian, C. Jiang, Thermal relaxation of residual stresses in shot peened surface layer of SiCw/Al composite, *J. Mater. Eng. Perform.* 21 (2012) 915–919.
- [64] W. Luan, C. Jiang, V. Ji, Thermal relaxation of residual stresses in shot peened surface layer on TiB₂/Al composite at elevated temperatures, *Mater. Trans.* 50 (2009) 1499–1501.